Centennial-scale climate cooling with a sudden cold event around 8,200 years ago

Eelco J. Rohling & Heiko Pälike

Southampton Oceanography Centre, Southampton SO14 3ZH, UK

....

The extent of climate variability during the current interglacial period, the Holocene, is still debated. Temperature records derived from central Greenland ice cores show one significant temperature anomaly between 8,200 and 8,100 years ago, which is often attributed to a meltwater outflow into the North Atlantic Ocean and a slowdown of North Atlantic Deep Water formation—this anomaly provides an opportunity to study such processes with relevance to present-day freshening of the North Atlantic. Anomalies in climate proxy records from locations around the globe are often correlated with this sharp event in Greenland. But the anomalies in many of these records span 400 to 600 years, start from about 8,600 years ago and form part of a repeating pattern within the Holocene. More sudden climate changes around 8,200 years ago appear superimposed on this longer-term cooling. The compounded nature of the signals implies that far-field climate anomalies around 8,200 years ago cannot be used in a straightforward manner to assess the impact of a slowdown of North Atlantic Deep Water formation, and the geographical extent of the rapid cooling event 8,200 years ago remains to be determined.

One notable cooling event between 8.25 and 8.15 thousand years before present (kyr BP) disrupts the remarkable stability of the Holocene epoch in temperature proxy data (ice $\delta^{18}O$) from the GISP2 Greenland ice core. The age models of the GRIP and North-GRIP Greenland ice cores place it at 8.15–8.05 kyr BP (Fig. 1, and Supplementary Information). The generally accepted explanation for this so-called '8.2-kyr-BP event' envisages curtailment of North Atlantic Deep Water (NADW) formation and its associated northward heat transport, due to a catastrophic meltwater release into the North Atlantic[1,2]. This notion was supported by dating of a final outburst drainage from glacial lakes Agassiz and Ojibway during the terminal demise of the Laurentide ice sheet, around 8.47 kyr BP (ref. 3). Because the 8.2-kyr-BP event occurred within the Holocene, it might hold clues about the potential response of NADW formation to the current freshening of the North Atlantic[4]. It is also unclear whether the 8.2-kyr-BP event was indeed associated with a significant NADW slowdown[5,6], which is thought to be a key mechanism for widespread climate impacts[7,8]. Clearly, a detailed assessment of the events around 8.2 kyr BP is essential.

Anomalies have been observed around 8.2 kyr BP in palaeoclimate archives on a near-global scale, except for the high southern latitudes[2,9–11]. Climate models forced with a strong freshwater pulse into the North Atlantic (leading to NADW slowdown) do suggest widespread consequences[7,8]. On that basis, it seems reasonable to view almost all anomalies observed in climate proxy records at roughly 8 kyr BP as evidence of this scenario for global climate change, ascribing any dating and duration differences to poor age control and resolution in other archives relative to Greenland ice cores[2]. Here we evaluate a selection of well-dated, highly resolved climate proxy records that have been developed since the initial reports. This evaluation bears directly upon: (1) the inferred cause for the 8.2-kyr-BP event; (2) the broader climatic context of the event; and (3) the global distribution of the event.
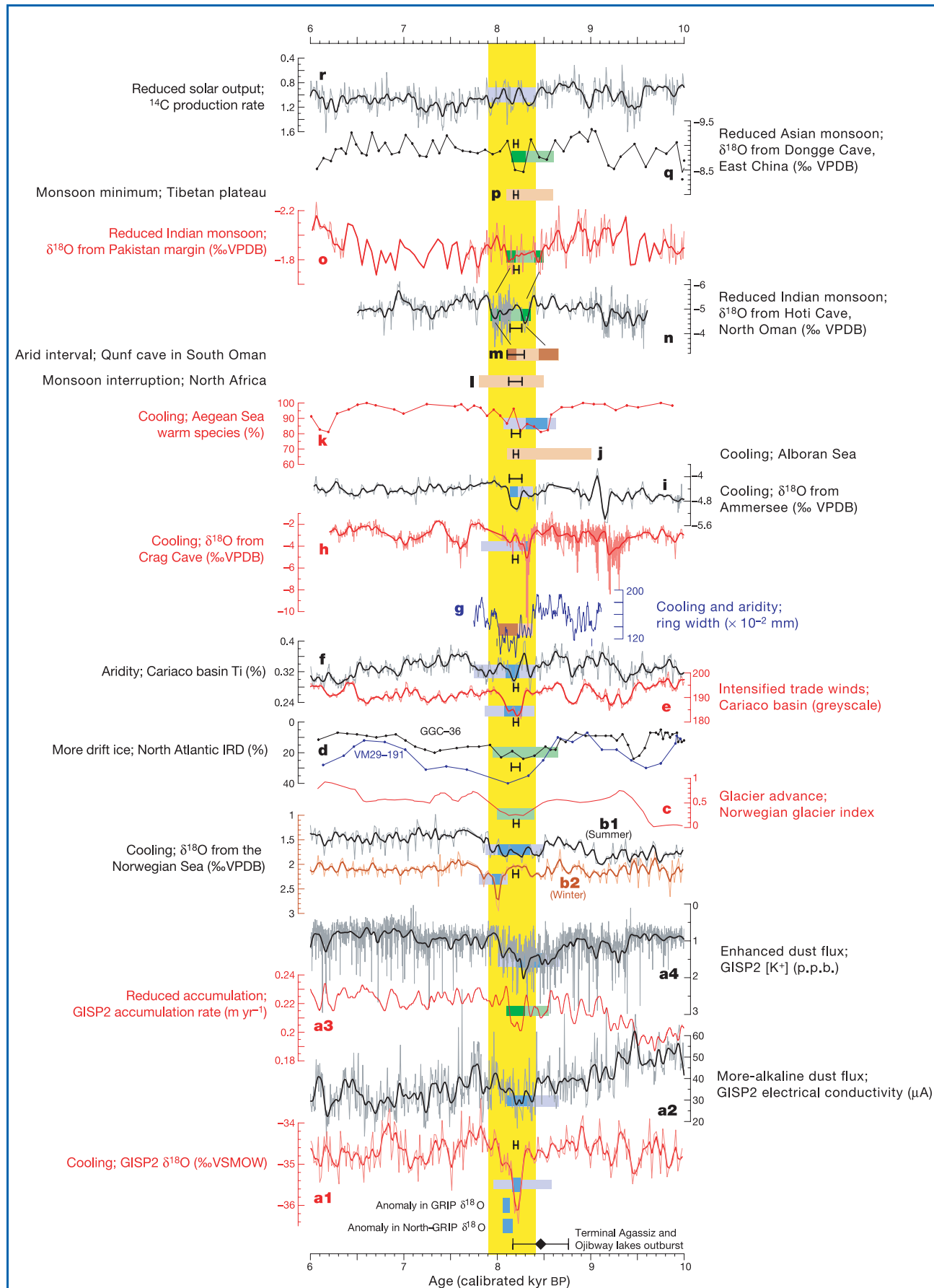
Anomalies in climate proxy records from Greenland

Sharp anomalies centred on about 8.2 kyr BP were found not only in ice $\delta^{18}O$ (Fig. 1a1), but also in other proxies (for example, chloride) from the Greenland ice cores[2]. However, other Greenland ice-core proxies show anomalies over a much longer time interval. This is best illustrated by the GISP2 potassium series, a proxy for dust supply to Greenland, which contains a broad maximum between

8.65 and 8.00 kyr BP (refs 9, 12; Fig. 1a4). All time intervals cited here are detailed in Supplementary Tables S1 and S2. GISP2 potassium maxima have been interpreted in terms of expansion and intensification of the atmospheric polar vortex[9,12]. Another proxy for alkaline dust supply to Greenland, electrical conductivity (ECM), also shows a compound maximum between 8.65 and 8.10 kyr BP, with a peak at 8.4–8.1 kyr BP (refs 13, 14) (Fig. 1a2). The GISP2 accumulation rate visually suggests a broad reduction between 8.55 and 8.1 kyr BP with a minimum at 8.3–8.1 kyr BP (Fig. 1a3), although this is not statistically significant (see Supplementary Information). These different proxies, co-registered in a single archive, clearly suggest that the sharp 8.2-kyr-BP event punctuated a longer-term background anomaly. The sharp peak is prominent in the $\delta^{18}O$ proxy for temperature at the Greenland summit, and the broader anomaly is apparent in proxies for the structure/intensity of atmospheric circulation.

Anomalies in climate proxy records around the North Atlantic

Throughout this region, the sharp 8.2-kyr-BP event, where present, again occurs within a broader anomaly (Fig. 1b–j). A particularly revealing case is portrayed by the anomalies in records b1 and b2 from a Norwegian Sea sediment core[15] (Fig. 1b1,b2). The typical sharp signature of the 8.2-kyr-BP event is found at 8.0–7.9 kyr BP in the $\delta^{18}O$ record of the left-coiling (sinistral) planktonic foraminifer *Neogloboquadrina pachyderma*, whereas a broad maximum between 8.5 and 7.9 kyr BP is revealed in the $\delta^{18}O$ of right-coiling (dextral) *N. pachyderma*[15]. These records are based on the same sample series, so there can be no argument about the different phasing and durations of the anomalies. The combination of both sharp and broad anomalies within a single archive offers sound evidence that the sharp 8.2-kyr-BP event occurred within a broad climate anomaly between about 8.6/8.5 and 8.0 kyr BP, similar to the pattern highlighted above for the GISP2 ice core. The Norwegian Sea record furthermore offers vital insight into the season-specific nature of the two anomalies, because the $\delta^{18}O$ record of sinistral *N. pachyderma* may reflect winter temperature, whereas that of dextral *N. pachyderma* may reflect summer temperature[15].

Stalagmite $\delta^{18}O$ data from the Irish Crag Cave[16,17] and carbonate $\delta^{18}O$ data from the German lake Ammersee[18] show a dominant sharp peak anomaly, at 8.35–8.3 and 8.2–8.15 kyr BP, respectively (Fig. 1h–i). These anomalies are (partly) explained in terms of enhanced isotopic fractionation in precipitation during the cold

Reduced solar output;
^{14}C production rate

Reduced Asian monsoon;
δ^{18}O from Dongge Cave,
East China (‰ VPDB)

Monsoon minimum; Tibetan plateau

Reduced Indian monsoon;
δ^{18}O from Pakistan margin (‰VPDB)

Reduced Indian monsoon;
δ^{18}O from Hoti Cave,
North Oman (‰ VPDB)

Arid interval; Qunf cave in South Oman

Monsoon interruption; North Africa

Cooling; Aegean Sea
warm species (%)

Cooling; Alboran Sea

Cooling; δ^{18}O from
Ammersee (‰ VPDB)

Cooling; δ^{18}O from
Crag Cave (‰VPDB)

Cooling and aridity;
ring width ($\times 10^{-2}$ mm)

Aridity; Cariaco basin Ti (%)

Intensified trade winds;
Cariaco basin (greyscale)

More drift ice; North Atlantic IRD (%)

GGC–36

VM29–191

Glacier advance;
Norwegian glacier index

Cooling; δ^{18}O from the
Norwegian Sea (‰VPDB)

b1 (Summer)

b2 (Winter)

Enhanced dust flux;
GISP2 [K$^+$] (p.p.b.)

Reduced accumulation;
GISP2 accumulation rate (m yr^{-1})

More-alkaline dust flux;
GISP2 electrical conductivity (μA)

Cooling; GISP2 δ^{18}O (‰VSMOW)

Anomaly in GRIP δ^{18}O

Anomaly in North-GRIP δ^{18}O

Terminal Agassiz and
Ojibway lakes outburst

Age (calibrated kyr BP)

8.2-kyr-BP event, in agreement with the strong and abrupt cooling seen over the North Atlantic region in climate models that simulate the impact of a meltwater flood[7,8]. Given that the Norwegian Sea records (Fig. 1b) identify the sharp cooling event as a winter phenomenon, it follows that the Crag Cave and Ammersee records are dominated by isotopic changes in winter precipitation.

The German tree ring width record shows a distinct low between 8.4 and 8.0 kyr BP, culminating in three sharp minima between 8.2 and 8.0 kyr BP (Fig. 1g), caused by colder and more arid climate conditions over central Europe[19]. This would agree with the broad period of reduced summer temperatures and superimposed sharp minimum winter temperatures in the Norwegian Sea. Annual temperatures at the Estonian lake Rõuge were reduced between about 8.5 and 8.1 kyr BP (culminating at 8.25–8.15 kyr BP), and erosion-related inorganic sedimentation was increased between 8.5 and 8.1 kyr BP with two sharp maxima at 8.3 and 8.2 kyr BP (ref. 20). These patterns mimic those in the tree-ring record (Fig. 1g), and agree with the substantial 'Finse' advance of Norwegian glaciers at 8.4–8.0 kyr BP (refs 21, 22; Fig. 1c). The Estonian cooling is marked by a decline in *Alnus* pollen, an indication of frost damage in early spring[20], which supports the inferred reduction of summer temperature after about 8.5 kyr BP in the Norwegian Sea. Reduced or seasonally delayed summer warming may also (partly) explain the glacier expansion, and would have facilitated the survival and dispersal of sea ice, which governed the Holocene ice-rafted debris (IRD) deposition. Although the initial IRD records showed only a broad maximum[23,24] (Fig. 1d), records of improved resolution have since revealed the culmination in a sharp IRD spike at the 8.2-kyr-BP event proper[25].

If there was an underlying climatic deterioration between about 8.5 and 8.0 kyr BP that was punctuated by the sharp 8.2-kyr-BP event, then we need to be very careful about attributing any anomaly around 8 kyr BP to the 8.2-kyr-BP event itself (as in refs 2, 7 and 17). It would instead be possible that the far-field correlations reflect the underlying climate anomaly, whereas the sharp signals triggered by the meltwater outburst were restricted to a much smaller (for

example, North Atlantic) realm. Archives from remote locations would then be likely to show well-dated anomalies that span four to six centuries, rather than a sharp event over about one century. Because monsoons are the most efficient means for interhemispheric vapour/latent heat transport, we pay specific attention to low- to mid-latitude records for evidence of monsoon variability. Given that the sharp 8.2-kyr-BP event may be most evident in winter-dominated proxies, and the broad underlying anomaly more characteristic of summer conditions, the seasonal significance of proxy records must be taken into account.

Anomalies in climate proxy records from monsoon regions

In the Cariaco basin, a broad multi-peak low in Ti percentages between 8.4 and 7.75 kyr BP reflects aridity due to reduced northward migration of the Intertropical Convergence Zone (ITCZ) in summer[26] (Fig. 1f). In contrast, a single sharp anomaly at 8.25–8.1 kyr BP in the greyscale record reflects enhanced intensities of the trade winds, which affect this region in winter[27] (Fig. 1e). This combination again portrays the different seasonal responses, with a broad anomaly in a summer-dominated proxy and a sharp event in a winter-dominated proxy.

A well-dated census of African summer-monsoon-fed lakes[28] illustrates a well-defined reduction in monsoon intensity or penetration between about 8.5 and 7.8 kyr BP (Fig. 1l) (a similar monsoon reduction exists within the previous (Eemian) interglaciation[29,30]). A broad Holocene monsoon minimum is also found in the Indian and Asian domains (Fig. 1m–q). Although strong high-frequency variability impedes statistical distinction of the centennial-scale signals in each record individually, records of Indian summer-monsoon intensity from around the Arabian Sea (Fig. 1m–o) show considerable visual similarity to one another[31–33], as well as with a marine $\delta^{18}O$ record from offshore Socotra Island[34]. Together, these records portray a broad reduction of Indian summer-monsoon activity between roughly 8.5 and 8.0 kyr BP, which both started and ended with a century-scale peak minimum (correlation lines in Fig. 1). There is a great lack of highly resolved

Figure 1 Collection of well-dated climate proxy records used to identify anomalies around 8.2 kyr BP. All records, including those from the ice cores, are presented versus 'calibrated age' in kyr BP, where 'before present' refers to before 1950. The records originate from ice cores, from laminated (usually anoxic) marine sediments, from marine sediments from other anoxic and/or high-accumulation settings that lack significant bioturbation, from cave stalactites or stalagmites and palaeo-lake deposits, and from a peat bog. All are all well dated using a variety of techniques from lamina/layer/varve counting to accelerator mass spectrometric (AMS) ^{14}C dating (including wiggle-matching), and U/Th dating. Error bars with the records portray the size of the one-sided 1σ uncertainty reported for the datings (see Supplementary Information Table S2). All smoothed records shown are based on a 50-yr moving gaussian filter. Coloured blocks identify the anomalies recognized in the various records: blue is statistically significant in digital records (see Supplementary Information); green is visually identified in digital records (not statistically significant); brown is estimated from published graphs. Heavy coloured blocks indicate peak events; lighter blocks highlight broader anomalies. The yellow band marks an interval spanning three conspicuous maxima in ^{14}C production. The black diamond with error bar alongside the age axis indicates the best age estimate for the meltwater flood from lakes Agassiz and Ojibway with 1σ bounds[3]. Axis labels identify the nature of the anomalies around 8 kyr BP.

Records are grouped by archive; each letter is a separate archive, and subnumbering refers to different proxies co-registered within that archive. Records **a1** to **a4** are all measured from the Greenland Ice Sheet Project II (GISP2) ice core: **a1** is the ice-$\delta^{18}O$ series[45], **a2** is the electrical conductivity series[13,14], **a3** is a 50-yr smoothing of the ice-accumulation data set[46] (actual data not shown to avoid clutter), and **a4** is the GISP2 potassium ion series[9,12] (spikes in actual data clipped at axis maximum value to avoid clutter). Also indicated are the timings of the sharp

$\delta^{18}O$ anomalies in the Greenland NorthGRIP and GRIP ice cores, which deviate slightly from that in GISP2 (**a1**) owing to small differences between the age models of the ice cores[47,48]. Records **b1** and **b2** are co-registered in a sediment core from the Norwegian Sea[15]: **b1** is $\delta^{18}O$ of right-coiling *Neogloboquadrina pachyderma*, **b2** is $\delta^{18}O$ of left-coiling *N. pachyderma*. Record **c** is a Norwegian glacier expansion index based on glacial lake cores investigated at a resolution better than 50 yr (Jostedalsbreen area) (ref. 21, and see also ref. 11). The two records in **d** show IRD percentages in North Atlantic sediment cores VM29-191 (54° N, 15° E) and GGC-36 (45° N, 45° E) (ref. 24). Records **e** and **f** are both from laminated sediment cores from the Cariaco basin: **e** shows greyscale measurements[27], and **f** shows titanium concentrations measured by core-logging X-ray fluorescence[26]. Record **g** (digitized) presents the German tree-ring-width series[19]. Record **h** is the Crag Cave $\delta^{18}O$ series[16,17], and **i** is the ostracod-based $\delta^{18}O$ series for Lake Ammersee[18]. Block **j** marks an interval of low sea surface temperatures in the Alboran Sea, westernmost Mediterranean[49], and record **k** does so for the Aegean Sea, northeastern Mediterranean[37]. Although of relatively low resolution, the Aegean record is kept within this evaluation because it is well dated and fully supported by a highly resolved (but less well-dated) record for the central Mediterranean[50]. Block **l** identifies the well-established, widespread interruption of the North African monsoon maximum[28], and **m** identifies an arid interlude with two distinct peaks reflected in stalagmite $\delta^{18}O$ for Qunf Cave in South Oman[31]. Record **n** is similar to **m**, but for Hoti Cave in North Oman[32]. Record **o** shows $\delta^{18}O$ of the surface-dwelling planktonic foraminifer *Globigerinoides ruber* in a laminated sediment core from the Pakistan margin[33]. Block **p** identifies a major interval of reduced monsoon activity identified from cellulose [33]in a peat-bog section in East Tibet[35], and record **q** is stalagmite $\delta^{18}O$ for Dongge Cave, East China[36]. Record **r** shows ^{14}C production rates from a recent deconvolution of the ^{14}C residuals series[41,42].

records from the Asian monsoon sector, but available speleothem and peat-bog records[35,36] suggest that a monsoon reduction also occurred there between roughly 8.6 and 8.1 kyr BP (Fig. 1p, q).

It cannot be excluded that part of the anomalies in the various low- to mid-latitude records might represent atmospheric or oceanic downstream effects of a meltwater pulse into the North Atlantic and its associated sharp cooling event. However, such a mechanism cannot explain the longer durations of the overall anomaly, or the fact that many records show a well-dated onset of climatic deterioration well before the sharp 8.2-kyr-BP event (Fig. 1, Supplementary Table S2). Note that there is a general lack of low- to mid-latitude records that reflect winter conditions, which might be more likely to show the sharp event than the available summer-dominated records, as illustrated by the data from the Cariaco basin (Fig. 1e, f).

Broad underlying climate anomaly

The early Holocene meltwater flood has been dated[3] at 8.47 ± 0.3 kyr BP (1σ). The oldest age for the onset of the sharp cooling in the Greenland ice cores is near 8.3 kyr BP. If it is related to an NADW slowdown due to meltwater addition, this constrains the age of the flood to within a couple of decades before 8.3 kyr BP (refs 7, 8), well within the 1σ bounds of the datings[3] and in close agreement with the age of 8.33 ± 0.08 kyr BP for the onset of the sharp climate impact in Ireland[16,17].

Climate models with a flood-related cold event of 200 yr suggest associated anomalies in other climate parameters that develop more gradually and may reach twice the duration, but none would start significantly before the flood or cold snap[8]. Evaluation of anomalies that lasted 400 yr or more in our compilation of proxy records (Fig. 1, Supplementary Table S2) shows that 90% (70%) started at or before 8.4 (8.5) kyr BP (Supplementary Table S2). This supports the pivotal observation from the co-registered signals in GISP2 and the Norwegian Sea that a widespread, multi-century climatic deterioration had started well before the flood-related cold event.

The independence of the longer-term anomalies from the meltwater flood is further illustrated by the fact that many are not unique within the Holocene. In GISP2, potassium maxima of comparable magnitude to that of 8.65–8.0 kyr BP are present at 6–5 kyr BP, 3.5–2.5 kyr BP, and AD 1400–1900 (the Little Ice Age), and correlative anomalies have been found outside Greenland[9,11,12,37]. Spurk et al.[19] report a recurrence of tree-ring-width minima similar to that of 8.4–8.0 kyr BP (for example, at 6.1–5.8 kyr BP), which they relate to repeated Holocene IRD episodes[23,24] and interpret in terms of a recurrent cycle of climatic deteriorations whose impact was amplified around 8.2 kyr BP by the meltwater flood.

Signal comparison between IRD records and the cosmogenic ^{14}C and [10]Be records suggests that the repeated Holocene climate deteriorations correspond to intervals of reduced solar output[23], corroborating similar inferences made previously[9,38,39]. Although high-frequency variability in the Earth's magnetic field might have some influence on cosmogenic isotope production[40], the solar variability hypothesis is gaining increasing support. [14]C production rates[41,42] reveal a conspicuous 500-yr interval with a succession of three broad ^{14}C production maxima (solar output minima) between 8.4 and 7.9 kyr BP (Fig. 1r). There is more than a passing resemblance with the succession of three ^{14}C production peaks between 0.7 and 0.2 kyr BP that spans the Little Ice Age. The interval of 8.4–7.9 kyr BP agrees well with the timing and duration of the broad climate deterioration highlighted here. The internal three-peak structure may be reflected by internal variability within this broad anomaly, supporting previous reports of remarkable peak-to-peak signal similarities between ^{14}C residuals and proxy records[31,32,34].

Compound climate signals around 8.2 kyr BP

The listed evidence for a multi-century climate deterioration, with an onset well before the meltwater flood of about 8.3 kyr ago, indicates that it would be erroneous to attribute all anomalies in climate proxy records around 8 kyr BP to the 8.2-kyr-BP event, in an attempt to map the global impacts of a slowdown in NADW production. Proxies for changes in the meridional extent of major atmospheric circulation features (polar vortex, ITCZ) seem more likely to reflect the underlying deterioration of about 8.5–8.0 kyr ago. In addition, this broad anomaly seems especially evident in summer-biased proxies, and the sharp 8.2-kyr-BP event more evident in winter-biased proxies.

The climate deterioration of about 8.5–8.0 kyr BP is part of a repeating pattern of longer-term anomalies during the Holocene, with its most recent manifestation during the Little Ice Age. It seems related to solar output fluctuations. Climate models for evaluation of the impacts of small reductions in solar output indicate notable impacts on the meridional structure of the atmospheric circulation[43,44], in broad agreement with the changes inferred from proxy data, but completely independent from any changes in NADW formation.

Our assessment indicates that the actual geographic extent of the sharp meltwater-induced 8.2-kyr-BP event remains to be established outside the circum-North-Atlantic region, which notably requires the development of new (winter-typical) proxy records in low to middle latitudes. This is especially important if climate proxy signals pertaining to the event are to be used to validate models of NADW slowdown, within the context of discussions on potential changes in deepwater formation in a greenhouse future. □

1. De Vernal, A., Hillaire-Marcel, C., Von Grafenstein, U. & Barber, D. Researchers look for links among paleoclimate events. Eos 78, 247–249 (1997).
2. Alley, R. B. et al. Holocene climatic instability: A large event 8000–8400 years ago. Geology 25, 482–486 (1997).
3. Barber, D. C. et al. Forcing of the cold event of 8,200 years ago by catastrophic drainage of Laurentide lakes. Nature 400, 344–348 (1999).
4. Curry, R., Dickson, B. & Yashayaev, I. A change in the freshwater balance of the Atlantic Ocean over the past four decades. Nature 426, 826–829 (2003).
5. Weaver, A. J. & Hillaire-Marcel, C. Global warming and the next ice age. Science 304, 400–402 (2004).
6. Kuijpers, A. et al. Late Quaternary sedimentary processes and ocean circulation changes at the Southeast Greenland margin. Mar. Geol. 195, 109–129 (2003).
7. Renssen, H., Goosse, H. & Fichefet, T. Modelling the effect of freshwater pulses on the early Holocene climate: the influence of high-frequency climate variability. Paleoceanography 17, doi:10.1029/2001PA000649 (2002).
8. Bauer, E., Ganopolski, A. & Montoya, M. Simulation of the cold climate event 8200 years ago by meltwater outburst from Lake Agassiz. Paleoceanography 19, doi:10.1029/2004PA001030 (2004).
9. O'Brien, S. R. et al. Complexity of Holocene climate as reconstructed from a Greenland ice core. Science 270, 1962–1964 (1995).
10. DeMenocal, P., Ortiz, J., Guilderson, T. & Sarnthein, M. Abrupt onset and termination of the African humid period: rapid climate responses to gradual insolation forcing. Quat. Sci. Rev. 19, 347–361 (2000).
11. Mayewski, P. A. et al. Holocene climate variability. Quat. Res. 62, 243–255 (2004).
12. Mayewski, P. A. et al. Major features and forcing of high latitude northern hemisphere atmospheric circulation using a 110,000-year-long glaciochemical series. J. Geophys. Res. 102, 26345–26366 (1997).
13. Taylor, K. C. et al. Ice core dating and chemistry by direct current electrical conductivity. J. Glaciol. 38, 325–332 (1992).
14. Taylor, K. C. et al. The 'flickering switch' of late Pleistocene climate change. Nature 361, 432–436 (1993).
15. Risebrobakken, B., Jansen, E., Andersson, C., Mjelde, E. & Hevrøy, K. A high-resolution study of Holocene paleoclimatic and paleoceanographic changes in the Nordic Seas. Paleoceanography 18, doi:10.1029/2002PA000764 (2003).
16. McDermott, F., Mattey, D. O. & Hawkesworth, C. Centennial-scale Holocene climate variability revealed by a high-resolution speleothem δ^{18}O record from SW Ireland. Science 294, 1328–1331 (2001).
17. Baldini, J. U., McDermott, F. & Fairchild, I. J. Structure of the 8200-year cold event revealed by a speleothem trace element record. Science 296, 2203–2206 (2002).
18. Von Grafenstein, U., Erlenkeuser, H., Brauer, A., Jouzel, J. & Johnsen, S. J. A mid-European decadal isotope-climate record from 15,500 to 5000 years B.P. Science 284, 1654–1657 (1999).
19. Spurk, M., Leuschner, H. H., Baillie, M. G. L., Briffa, K. R. & Friedrich, M. Depositional frequency of German subfossil oaks: climatically and non-climatically induced fluctuations in the Holocene. Holocene 12, 707–715 (2002).
20. Veski, S., Seppä, H. & Ojala, A. E. K. Cold event at 8200 yr B.P. recorded in annually laminated lake sediments in eastern Europe. Geology 32, 681–684 (2004).
21. Nesje, A., Matthews, J. A., Dahl, S. O., Berrisford, M. S. & Andersson, C. Holocene glacier fluctuations of Flatbreen and winter-precipitation changes in the Jostedalsbreen region, western Norway, based on glaciolacustrine sediment records. Holocene 11, 267–280 (2001).

22. Nesje, A., Dahl, S. O. & Bakke, J. Were abrupt Late glacial and early-Holocene climatic changes in northwest Europe linked to freshwater outbursts to the North Atlantic and Arctic Oceans? *Holocene* **14,** 299–310 (2004).

23. Bond, G. *et al.* Persistent solar influence on north Atlantic climate during the Holocene. *Science* **294,** 2130–2136 (2001).

24. Bond, G. *et al.* A pervasive millennial-scale cycle in North Atlantic Holocene and Glacial climates. *Science* **278,** 1257–1266 (1997).

25. Moros, M. *et al.* Sea surface temperatures and ice rafting in the Holocene North Atlantic: climate influences on northern Europe and Greenland. *Quat. Sci. Rev.* **23,** 2113–2126 (2004).

26. Haug, G. H., Hughen, K. A., Peterson, L. C., Sigman, D. M. & Röhl, U. Southward migration of the Intertropical Convergence Zone through the Holocene. *Science* **293,** 1304–1308 (2001).

27. Hughen, K. A., Overpeck, J. T., Peterson, L. C. & Trumbore, S. Rapid climate changes in the tropical Atlantic region during the last deglaciation. *Nature* **380,** 51–54 (1996).

28. Gasse, F. Hydrological changes in the African tropics since the last glacial maximum. *Quat. Sci. Rev.* **19,** 189–211 (2000).

29. Rohling, E. J. *et al.* African monsoon variability during the previous interglacial maximum. *Earth Planet. Sci. Lett.* **202,** 61–75 (2002).

30. Rohling, E. J. *et al.* Reconstructing past planktic foraminiferal habitats using stable isotope data: a case history for Mediterranean sapropel S5. *Mar. Micropaleontol.* **50,** 89–123 (2004).

31. Fleitmann, D. *et al.* Holocene forcing of the Indian monsoon recorded in a stalagmite from Southern Oman. *Science* **300,** 1737–1739 (2003).

32. Neff, U. *et al.* Strong coherence between solar variability and the monsoon in Oman between 9 and 6 kyr ago. *Nature* **411,** 290–293 (2001).

33. Staubwasser, M., Sirocko, F., Grootes, P. M. & Erlenkeuser, H. South Asian monsoon climate change and radiocarbon in the Arabian Sea during early and middle Holocene. *Paleoceanography* **17,** doi:10.1029/2000PA000608 (2002).

34. Jung, S. J. A., Davies, G. R., Ganssen, G. & Kroon, D. Decadal-centennial scale monsoon variations in the Arabian Sea during the early Holocene. *Geochem. Geophys. Geosyst.* **3,** doi:10.1029/ 2002GC000348 (2002).

35. Hong, Y. T. *et al.* Correlation between Indian Ocean summer monsoon and North Atlantic climate during the Holocene. *Earth Planet. Sci. Lett.* **211,** 371–380 (2003).

36. Yuan, D. *et al.* Timing, duration, and transitions of the Last Interglacial Asian monsoon. *Science* **304,** 575–578 (2004).

37. Rohling, E. J., Mayewski, P. A., Hayes, A., Abu-Zied, R. H. & Casford, J. S. L. Holocene atmosphere-ocean interactions: records from Greenland and the Aegean Sea. *Clim. Dyn.* **18,** 587–593 (2002).

38. Denton, G. H. & Karlen, W. Holocene climatic variations—Their pattern and possible cause. *Quat. Res.* **3,** 155–205 (1973).

39. Van Geel, B. *et al.* The role of solar forcing upon climate change. *Quat. Sci. Rev.* **18,** 331–338 (1999).

40. St-Onge, G., Stoner, J. S. & Hillaire-Marcel, C. Holocene paleomagnetic records from the St. Lawrence estuary, eastern Canada: centennial- to millennial-scale geomagnetic modulation of cosmogenic isotopes. *Earth Planet. Sci. Lett.* **209,** 113–130 (2003).

41. Muscheler, R., Beer, J. & Vonmoos, M. Causes and timing of the 8200 yr BP event inferred from the comparison of the GRIP ^{10}Be and the tree ring Δ^{14}C record. *Quat. Sci. Rev.* **23,** 2101–2111 (2004).

42. Muscheler, R., Beer, J., Kubik, P. W. & Synal, H. A. Geomagnetic field intensity during the last 60,000 years based on ^{10}Be and ^{36}Cl from the Summit ice cores and ^{14}C. *Quat. Sci. Rev.* (in the press).

43. Haigh, J. D. The impact of solar variability on climate. *Science* **272,** 981–984 (1996).

44. Shindell, D., Rind, D., Balachandran, N., Lean, J. & Lonergan, P. Solar cycle variability, ozone, and climate. *Science* **284,** 305–308 (1999).

45. Grootes, P. M., Stuiver, M., White, J. W. C., Johnsen, S. J. & Jouzel, J. Comparison of oxygen isotope records from the GISP2 and GRIP Greenland ice cores. *Nature* **366,** 552–554 (1993).

46. Cuffey, K. M. & Clow, G. D. Temperature, accumulation, and ice sheet elevation in central Greenland through the last deglacial transition. *J. Geophys. Res.* **102,** 26383–26396 (1997).

47. NGRIP members. High-resolution record of Northern Hemisphere climate extending into the last interglacial period. *Nature* **431,** 147–151 (2004).

48. Johnsen, S. *et al.* Irregular glacial interstadials recorded in a new Greenland ice core. *Nature* **359,** 311–313 (1992).

49. Cacho, I., Grimalt, J. O. & Canals, M. Response of the Western Mediterranean Sea to rapid climatic variability during the last 50,000 years: a molecular biomarker approach. *J. Mar. Syst.* **33–34,** 253–272 (2002).

50. Sprovieri, R., Di Stefano, E., Incarbona, A. & Gargano, M. E. A high-resolution record of the last deglaciation in the Sicily Channel based on foraminifera and calcareous nannofossil quantitative distribution. *Palaeogeogr. Palaeoclimatol. Palaeoecol.* **202,** 119–142 (2003).

Correspondence and requests for materials should be addressed to E.J.R. (E.Rohling@soc.soton.ac.uk).

Supplementary Information

Centennial-scale climate deterioration with a superimposed cold snap around 8,200 years ago

Eelco J. Rohling and Heiko Pälike
Southampton Oceanography Centre, Southampton SO14 3ZH, United Kingdom

The records that were digitally available for this study have been investigated statistically to identify significant anomalies of multi-centennial duration between 9 and 7 ka BP, and of decadal to centennial duration around 8 ka BP. This was done as follows:

The aim of the analysis is to identify, in a quantitative way, excursions in time series that stand out from the background noise. A typical approach would be to apply some level of smoothing to a given data set, assuming that any independent noise is reduced during this process. However, this requires the a priori selection of a smoothing interval. This is also an objection for more intricate kernel smoothers of data that apply a fixed smoothing interval, or bandwidth. Features found in data sets depend on the level of detail for which the time series is smoothed and analysed, and the question is which features observed in a smooth are really there, and what is the optimum bandwidth to apply for smoothing?

To avoid a priori bandwidth selection, we instead applied a scale-space technique[s1] where detection of significant features is conducted over all possible bandwidths. The kernel-based smoothing approach is entitled SiZer (Significant Zero crossings of derivatives). In this method, a family of smoothing curves with varying bandwidths are computed for a given data set. From the family of smoothing curves, the first and second derivatives are calculated, using MATLAB software[s2], from which statistics are calculated.

From the derivatives for the smoothings at varying bandwidths, statistically significant regions of positive and negative slopes, as well as statistically significant ridges and troughs are calculated (we chose an 85% confidence level, but there is no large difference with other confidence levels). The results are shown in Figure *S1*. For all analyses, 801 bins along the age axis were calculated, resulting in an average age resolution of ca. 14 yrs for the 11.5 kyr long records.

From the numerical results, we determined bandwidths which show statistically significant negative and positive slopes around 8.2 kyr, and statistically significant second derivative crossings (ridges or troughs). Bandwidths were picked to capture the longest and shortest possible scales and are summarised in Table *S1*, and indicated as horizontal black lines on Figure *S1*. For the slope (1st derivate) analysis, ages were determined between mid-points of statistically significant upward and downward curvatures. For the centre panel ("Slope SiZer Map") of Figure *S1*, significant upward (positive) slopes are indicated by the darkest shade, downward (negative) ones by the lightest shade. Fore the curvature analysis, statistically significant ridges or troughs were determined from start to end from the lower panel of Figure *S1* ("Curvature SiZer Map"), where the darkest shade corresponds to a statistically significant positive curvature ("trough"), whereas the lightest shade corresponds to a statistically significant negative curvature ("ridge").

In the following, Table *S1* shows the results of statistical assessment of the digitally available records, Table *S2* shows the characteristics of the records presented in main-text Figure 1, with the identified minimum and maximum age-intervals for the anomalies and the uncertainties reported for the various dating techniques. Figure *S1* presents graphs for the results of the statistical analyses.

CAPTIONS

Table *S1*. Summary of statistically significant excursions around 8.2 kyr that stand out from the background noise, obtained by statistical analysis of curvatures and slopes from "family of smooths" [s1]. Record labels correspond to main-text Figure 1. Symbols + and - indicate whether ridges or troughs were determined, using more positive data values along the ordinate axis. "Range" specifies age range of analysis. For all analyses, 801 bins along the age axis were calculated, resulting in an average age resolution for the ages given of ca. 14 yrs for the 11.5 kyr long records. Bandwidths are given for which curvatures and slopes were taken, corresponding to horizontal lines in the set of Figure *S1*. For the slope (1st derivate) analysis, ages were determined between mid-points of statistically significant upward and downward curvatures. For the centre panel ("Slope SiZer Map") of Figure *S1*, significant upward (positive) slopes are indicated by the darkest shade, downward (negative) ones by the lightest shade. Fore the curvature analysis, statistically significant ridges or troughs were determined from start to end from the lower panel of Figure *S1* ("Curvature SiZer Map"), where the darkest shade corresponds to a statistically significant positive curvature ("trough"), whereas the lightest shade corresponds to a statistically significant negative curvature ("ridge"). Length and central age were determined from the young and old ages. For dataset "r" only, we determined three individual excursions using the curvature, and a wider range encompassing these three excursions with the slope method. Bold marking indicates the intervals used in Table *S2* and main-text Figure 1. The asterisk with the Pakistan margin results indicates the fact that although a (not very well defined (Figure *S1*)) significant anomaly was detected, a visual identification was preferred to highlight the strong signal similarity with other records from around the Arabian Sea (see main-text Figure 1).

Table *S2*. Details of the records and the anomalies around 8.2 ka BP as highlighted in main-text Figure 1. The intervals for the "long anomaly" and "sharp 8.2 ka BP event" are the longest and shortest intervals identified from the two statistical criteria (see above, Table *S1*, and Figure *S1*). When selecting from the statistical analyses (Table *S1*) the length of the centennial-scale long anomaly, we have focussed on anomalies shorter than 750 years, i.e. less than half the period of the Holocene "1500 year" cycle[23,24], to avoid confusion with millennial-scale fluctuations. Colours correspond to the scheme used in main-text Figure 1. Blue refers to statistically significant anomalies in digitally available records (see Table *S1*), green refers to visual identification in digitally available records (not statistically significant), and brown refers to anomalies identified in published graphs.

Figure *S1*. Results of statistical SiZer analysis[s1] for the digital data sets used in main-text Figure 1. For each data set, three panels are shown. The upper panel shows the raw data, together with a family of computed smoothing curves. Three of the smooths are plotted in black and correspond to selected bandwidths that were used for Table *S1*. The middle panel shows the results of a slope analysis of the family of smooths. The ordinate (y) axis is the logarithm of the bandwidth (in kyr), the horizontal axis shows age. Significant upward

2

(positive) slopes are indicated by the darkest shade, downward (negative) ones by the lightest shade. The lower panel shows the results of the curvature (2nd derivative) analysis. The darkest shade corresponds to a statistically significant positive curvature ("trough"), whereas the lightest shade corresponds to a statistically significant negative curvature ("ridge").

References
(normal numbers correspond to the main-text references; "s" numbered references refer to those given below)

s1. Chaudhuri, P. & Marron, J. S. SiZer for Exploration of Structures in Curves. *J. Am. Statistic. Soc.* **94**, 807–823 (1999).
s2. Marron, J. S. Introduction to SiZer, http://www.stat.unc.edu/faculty/marron/ DataAnalyses/SiZer_Intro.html. Cited 09 December 2004
s3. Gasse, F. Diatom-inferred salinity and carbonate oxygen isotopes in Holocene waterbodies of the western Sahara and Sahel (Africa). *Quat. Sci. Rev.* **21**, 737-767 (2002).

Table *S1*.

Label	Data set	ridge(+)/ trough(-)	Range young (kyr)	old	Band-width (kyr)	Slope analysis (85% confidence) young (kyr)	old	length	centre	Curvature analysis (85% confidence) young (kyr)	old	length	centre
	GRIP-d18O	-	0.0	11.5	0.30	7.806	8.568	0.762	8.187	7.935	8.366	0.431	8.151
	GRIP-d18O	-	0.0	11.5	0.20	7.863	8.352	0.489	8.108	7.964	8.223	0.259	8.094
	GRIP-d18O	-	0.0	11.5	0.07	7.978	8.179	0.201	8.079	**8.064**	**8.136**	**0.072**	**8.100**
	NorthGrip		0.0	11.5	0.30					**8.064**	**8.309**	**0.245**	**8.187**
	NorthGrip	-	0.0	11.5	0.20					8.036	8.237	0.201	8.137
	NorthGrip	-	0.0	11.5	0.08					**8.064**	**8.165**	**0.101**	**8.115**
a1	GISP2-d18O	-	0.0	11.5	0.30	**7.964**	**8.582**	**0.618**	**8.273**	8.079	8.453	0.374	8.266
a1	GISP2-d18O	-	0.0	11.5	0.20	7.978	8.510	0.532	8.244	8.079	8.352	0.273	8.216
a1	GISP2-d18O	-	0.0	11.5	0.07	8.064	8.294	0.230	8.179	**8.165**	**8.251**	**0.086**	**8.208**
a2	GISP2_ECM	-	0.0	11.5	0.30					**8.136**	**8.654**	**0.518**	**8.395**
a2	GISP2_ECM	-	0.0	11.5	0.20					**8.108**	**8.381**	**0.273**	**8.245**
a2	GISP2_ECM	-	0.0	11.5	0.08	8.108	8.539	0.431	8.324				
a3	GISP2_accumrate		0.0	11.5		Not determined by this method with statistical significance							
a4	GISP2_K	+	0.0	11.5	0.30					8.108	8.611	0.503	8.360
a4	GISP2_K	+	0.0	11.5	0.20	8.021	8.668	0.647	8.345	**8.194**	**8.510**	**0.316**	**8.352**
a4	GISP2_K	+	0.0	11.5	0.06	**8.007**	**8.668**	**0.661**	**8.338**				
b1	Norw. Sea winter	-	0.0	11.5	0.30								
b1	Norw. Sea winter	-	0.0	11.5	0.11	**7.806**	**8.108**	**0.302**	**7.957**	7.949	8.021	0.072	7.985
b1	Norw. Sea winter	-	0.0	11.5	0.08					8.305	8.400	0.095	8.353
b2	Norw. Sea summer	+	0.0	11.5	0.30					8.007	8.366	0.359	8.187
b2	Norw. Sea summer	+	0.0	11.5	0.28					**8.007**	**8.352**	**0.345**	**8.180**
b2	Norw. Sea summer	+	0.0	11.5	0.14	**7.878**	**8.496**	**0.618**	**8.187**				
e	Cariaco_grey	-	0.0	11.5	0.30	**7.863**	**8.395**	**0.532**	**8.129**	7.935	8.366	0.431	8.151
e	Cariaco_grey	-	0.0	11.5	0.20	7.964	8.395	0.431	8.180	7.993	8.352	0.359	8.173
e	Cariaco_grey	-	0.0	11.5	0.04	8.064	8.380	0.316	8.222	**8.079**	**8.266**	**0.187**	**8.173**
f	Cariaco_Ti	-	0.0	11.5	0.30	**7.748**	**8.409**	**0.661**	**8.079**	7.834	8.309	0.475	8.072
f	Cariaco_Ti	-	0.0	11.5	0.20	7.748	8.366	0.618	8.057	7.820	8.208	0.388	8.014
f	Cariaco_Ti	-	0.0	11.5	0.05	**8.093**	**8.237**	**0.144**	**8.165**				
h	Crag_cave	-	0.0	10.1	0.30	**7.828**	**8.345**	**0.517**	**8.087**	7.966	8.269	0.303	8.118
h	Crag_cave	-	0.0	10.1	0.20	7.979	8.383	0.404	8.181	8.055	8.307	0.252	8.181
h	Crag_cave	-	0.0	10.1	0.03	7.966	8.408	0.442	8.187	**8.295**	**8.333**	**0.038**	**8.314**
i	Ammersee	-	0.0	11.5	0.30					8.209	8.340	0.131	8.275
i	Ammersee	-	0.0	11.5	0.20					**8.150**	**8.376**	**0.226**	**8.263**
i	Ammersee	-	1.5	11.0	0.08					**8.138**	**8.221**	**0.083**	**8.180**
k	Aegean	-	0.0	11.5	0.30	7.863	8.812	0.949	8.338	8.136	9.596	1.460	8.866
k	Aegean	-	0.0	11.5	0.20	7.820	8.869	1.049	8.345	**8.064**	**8.625**	**0.561**	**8.345**
k	Aegean	-	0.0	11.5	0.06	7.906	8.697	0.791	8.302	**8.309**	**8.539**	**0.230**	**8.424**
n	Hoti_cave		6.0	9.6		Not determined by this method with statistical significance							
o	Pakistan margin*	+	5.4	10.7	0.30					8.236	8.414	0.178	8.325
o	Pakistan margin*	+	5.4	10.7	0.24					8.249	8.421	0.172	8.335
o	Pakistan margin	+	5.4	10.7	0.06								
q	Dongge		0.0	11.5		Not determined by this method with statistical significance							
r	14Cproduction	+	6.0	10.0	0.06					7.906	8.036	0.130	7.971
r	14Cproduction	+	6.0	10.0	0.02	**7.905**	**8.41**	**0.505**	**8.158**	**7.915**	**7.940**	**0.025**	**7.928**
r	14Cproduction	+	6.0	10.0	0.02					**8.160**	**8.180**	**0.020**	**8.170**
r	14Cproduction	+	6.0	10.0	0.02					**8.320**	**8.335**	**0.015**	**8.328**
r	14Cproduction	+	6.0	10.0	0.01					8.320	8.335	0.015	8.328

4

Table S2.

Code in main-text Fig.1	Site	Proxy	Material type	Type of dating	Number of datings <12.5 kaBP	Reported 1σ of dating uncertainty around 8 ka BP (before wiggle match) (ky)	Character of event	Long anomaly. Age top, ka BP	Long anomaly. Age Base, ka BP	Long anomaly. Duration	Sharp "8.2 event". Age top, ka BP	Sharp "8.2 event". Age Base, ka BP	Sharp "8.2 event". Duration	Ref.
	North-GRIP	Ice δ^{18}O	Layered ice	Multi-proxy model	n/a	0.05	cooling				8.064	8.165	0.101	47
	GRIP	Ice δ^{18}O	Layered ice	Multi-proxy model	n/a	0.05	cooling				8.064	8.136	0.072	48
a1	GISP2	Ice δ^{18}O	Layered ice	Layer count	n/a	0.05	cooling	7.964	8.582	0.618	8.165	8.251	0.086	45
a2	GISP2	Electric Conductivity Measurement	Layered ice	Layer count	n/a	0.05	Conductivity minimum (dust maximum)	8.136	8.654	0.518	8.108	8.381	0.273	13,14
a3	GISP2	Accumulation rate	Layered ice	Layer count	n/a	0.05	accumulation minimum	8.1	8.55	0.450	8.1	8.3	0.200	46
a4	GISP2	[K$^+$]	Layered ice	Layer count	n/a	0.05	K+ maximum (dust)	8.007	8.668	0.661	8.194	8.510	0.316	9,12
b1	Norwegian Sea	δ^{18}O of N. pachyderma (dextral)	Marine sediment	AMS^{14}C + Vedde ash	12 + 1	0.06	summer cooling	7.878	8.496	0.618	8.007	8.352	0.345	15
b2	Norwegian Sea	δ^{18}O of N. pachyderma (sinistral)	Marine sediment	AMS^{14}C + Vedde ash	12 + 1	0.06	winter cooling	7.806	8.108	0.302	7.949	8.021	0.072	15
c	Norwegian glacier advance index	Various (esp. weight loss on ignition)	Glacial lake cores	AMS^{14}C	12	0.05	glacier expansion	8.0	8.4	0.400				21,22
d	Eastern N Atlantic	Petrological drift-ice tracers	Marine sediment	AMS^{14}C	20	0.10	drift-ice maximum	7.95	8.65	0.700				23
e	Cariaco Basin	[Ti]	Laminated marine sediment	AMS^{14}C	11	0.05	reduced runoff	7.748	8.409	0.661	8.093	8.237	0.144	26
f	Cariaco Basin	Grey scale	Laminated marine sediment	AMS^{14}C + varve count	51	0.05	increased trade winds	7.863	8.395	0.532	8.079	8.266	0.187	27
g	German tree-ring width record	Tree ring width	Tree rings	ring count	n/a		climatic deterioration	8.0	8.4	0.400	8.0	8.2	0.200	19
h	Crag Cave, Ireland	Speleothem δ^{18}O	Speleothem carbonate	U/Th	13	0.06	xxx	7.828	8.345	0.517	8.295	8.333	0.038	16,17
i	Ammersee, Germany	Ostracod δ^{18}O	Lake sediment	AMS^{14}C, tephra, correlation with varved record	4	0.13	cooling/ change in isotope fractionation	8.150	8.376	0.226	8.138	8.221	0.083	18

j	Alboran Sea	Alkenone SST	Marine sediment	AMS[14]C	10		cooling	8.10	9.00	0.900				49
k	Aegean Sea	Planktonic foraminiferal abundances	Anoxic marine sediment	AMS[14]C	9 (20)*	0.10	cooling	8.064	8.625	0.561	8.309	8.539	0.230	37
l	N African monsoon domain	Fossil lake levels	Lake sediments	AMS[14]C	89	0.10-0.20 (see also Ref. S1)	reduced monsoon intensity/ migration	7.80	8.50	0.700				28
m	Qunf cave, S. Oman	$\delta^{18}O$ of stalagmite carbonate	Stalagmite	U/Th	18	0.20	reduced monsoon intensity	8.10	8.65	0.550	8.10 also: 8.45	8.20 also: 8.65	0.100 / 0.200	31
n	Hoti cave, N. Oman	$\delta^{18}O$ of stalagmite carbonate	Stalagmite	U/Th	12	0.07-0.20	reduced monsoon intensity	7.95	8.35	0.400	7.95 also: 8.25	8.15 also: 8.35	0.200 / 0.100	32
o	Pakistan margin	$\delta^{18}O$ of G. *ruber*	Laminated marine sediment	AMS[14]C incl. wiggle-matching	49	0.05-0.07	reduced monsoon intensity	8.10	8.50	0.400	8.10 and: 8.40	8.20 and: 8.50	0.100 and: 0.100	33
p	Dongge cave (E. China)	$\delta^{18}O$ of stalagmite carbonate	Stalagmite	U/Th	19	0.05	reduced monsoon intensity	8.15	8.6	0.450	8.15	8.30	0.150	35
q	Hongyun peat bog E.Tibetan plateau	$\delta^{13}C$ of cellulose	Peat bog section	AMS[14]C	15	0.06	reduced monsoon intensity	8.10	8.60	0.500				36
r	[14]C production rate		Model deconvolution of ^{14}C residuals				reduced solar output	7.905	8.410	0.505	peaks centered on 7.915 - 7.940 8.160 – 8.180 8.320 – 8.335			41,42

* number including additional age control points from narrowly-constrained correlation with dated nearby cores
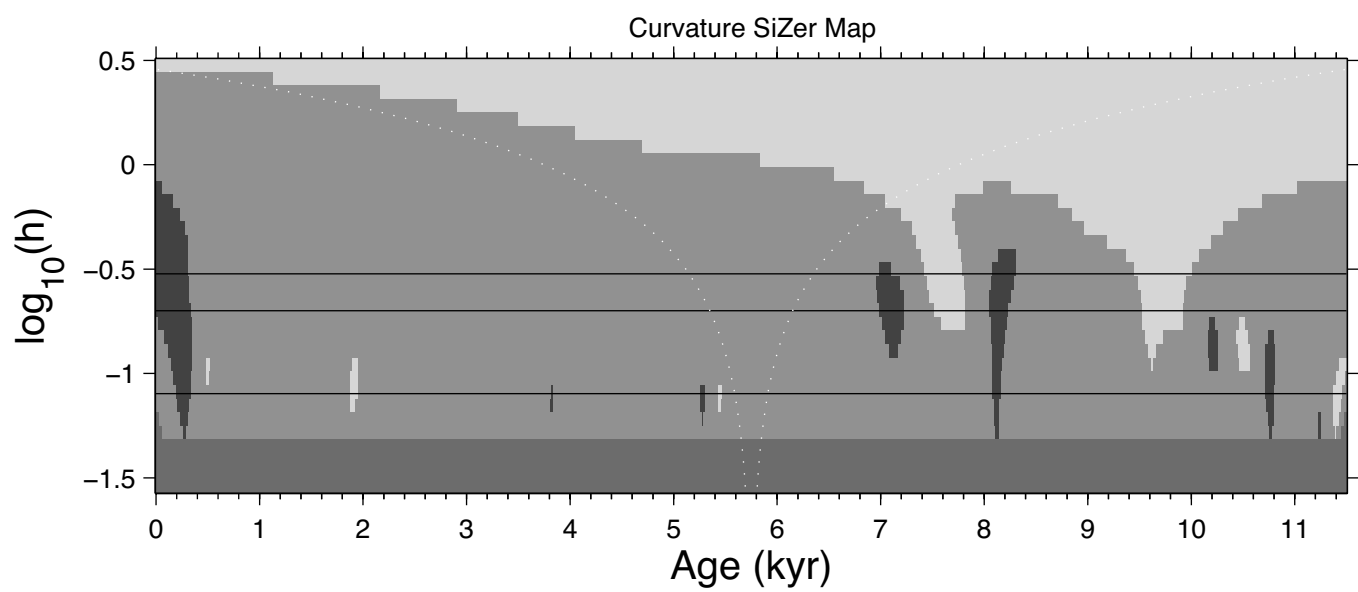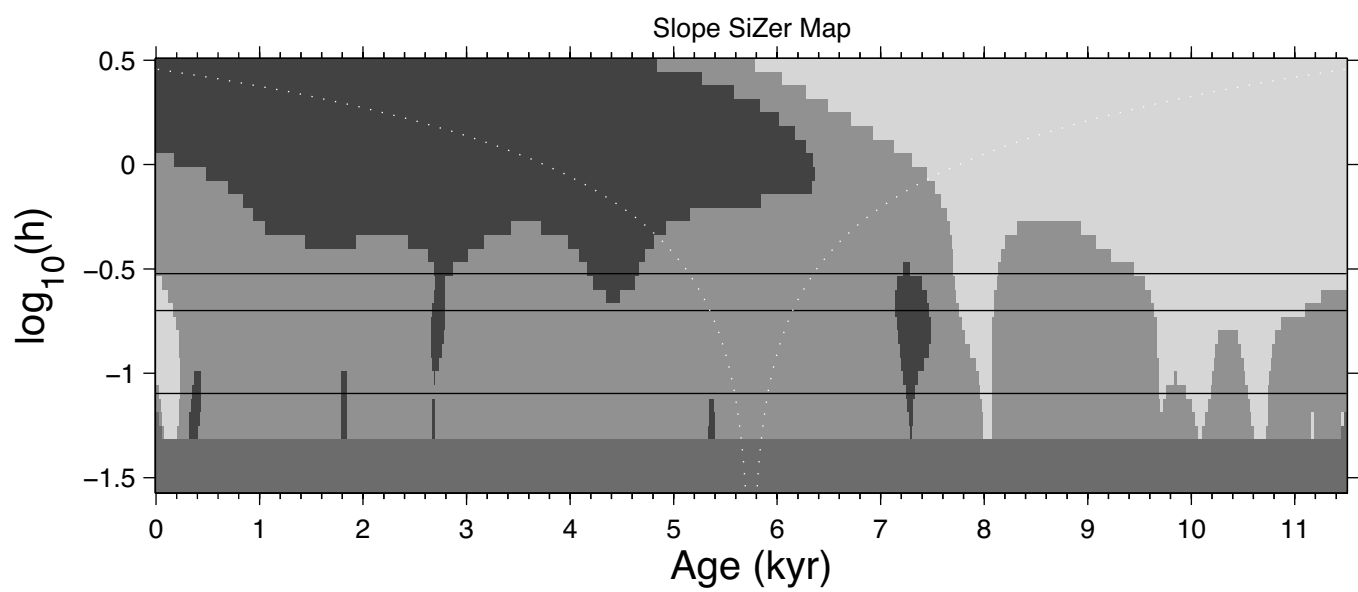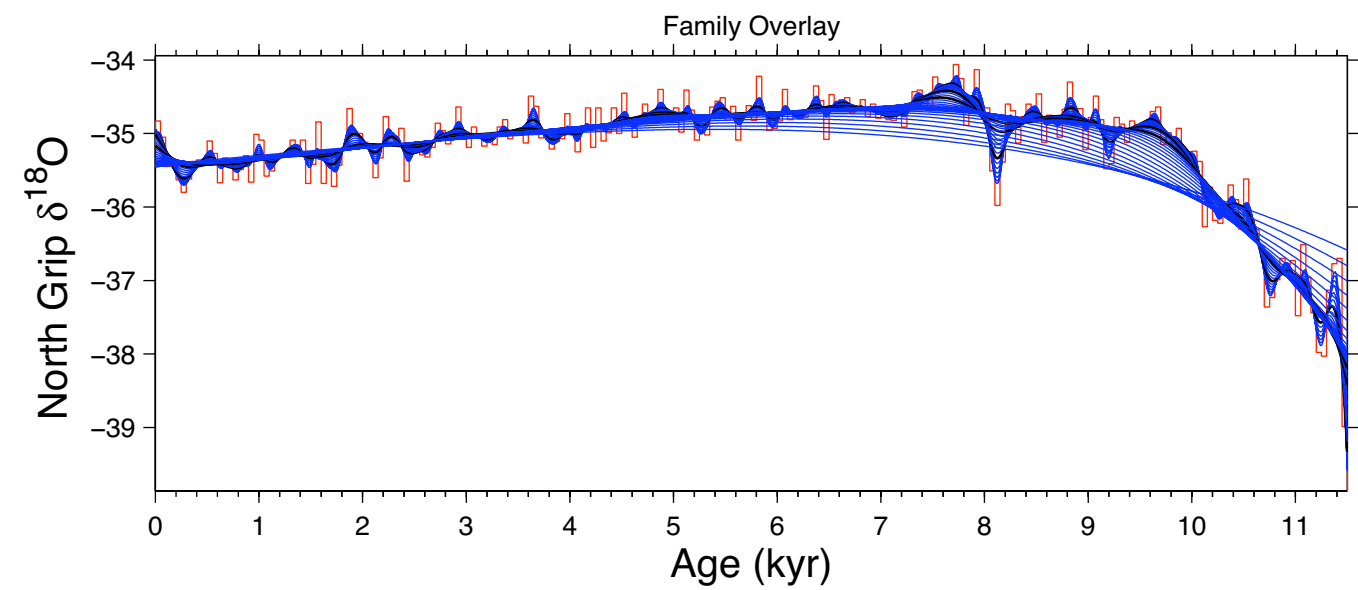
Figure S1

Figure S1 continued

Family Overlay

a1: GISP2 δ¹⁸O

Slope SiZer Map

Curvature SiZer Map

Figure S1 continued

Figure S1 continued

Figure S1 continued

Figure S1 continued

Family Overlay
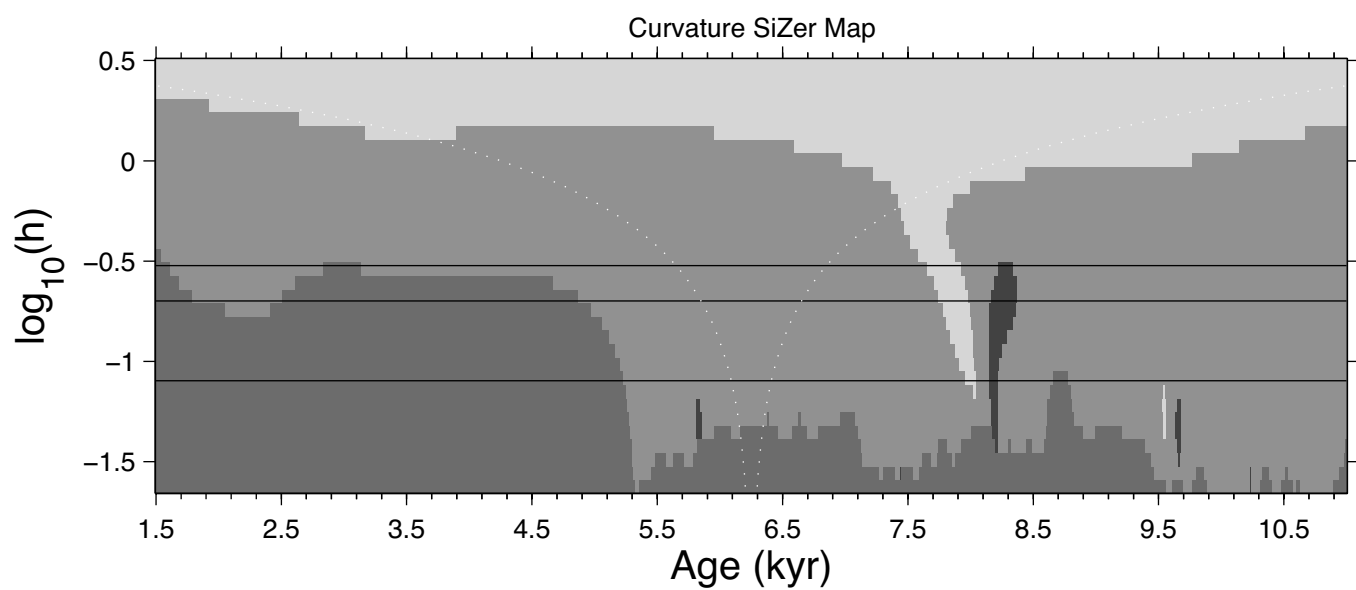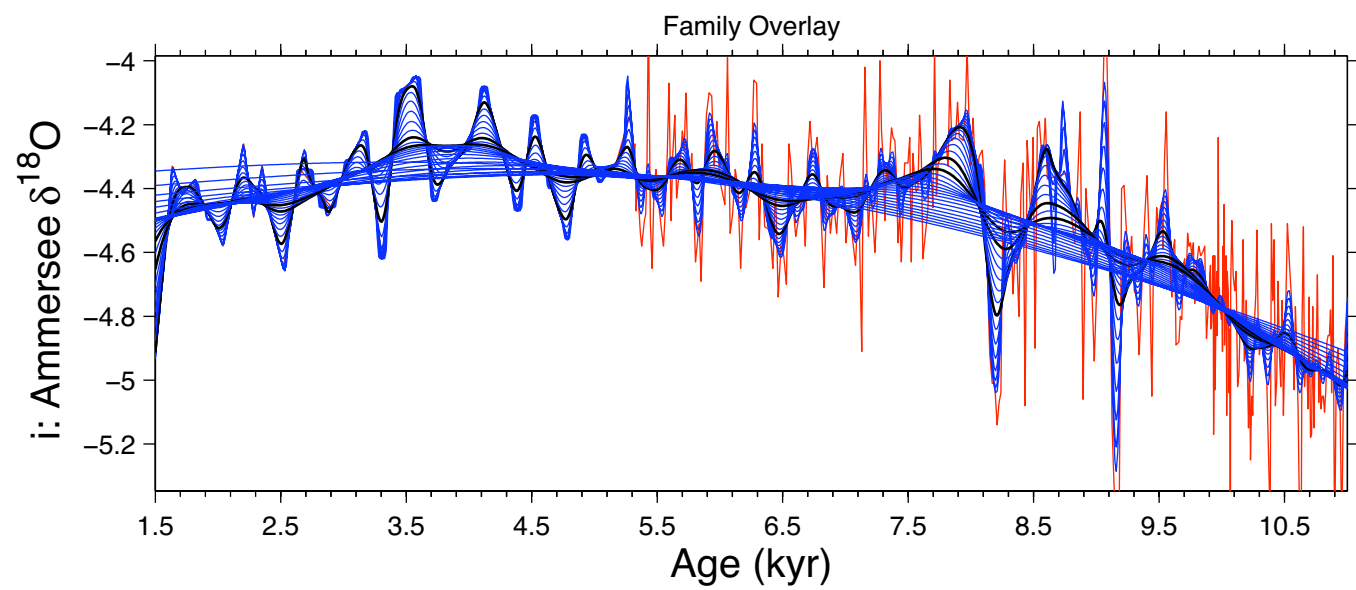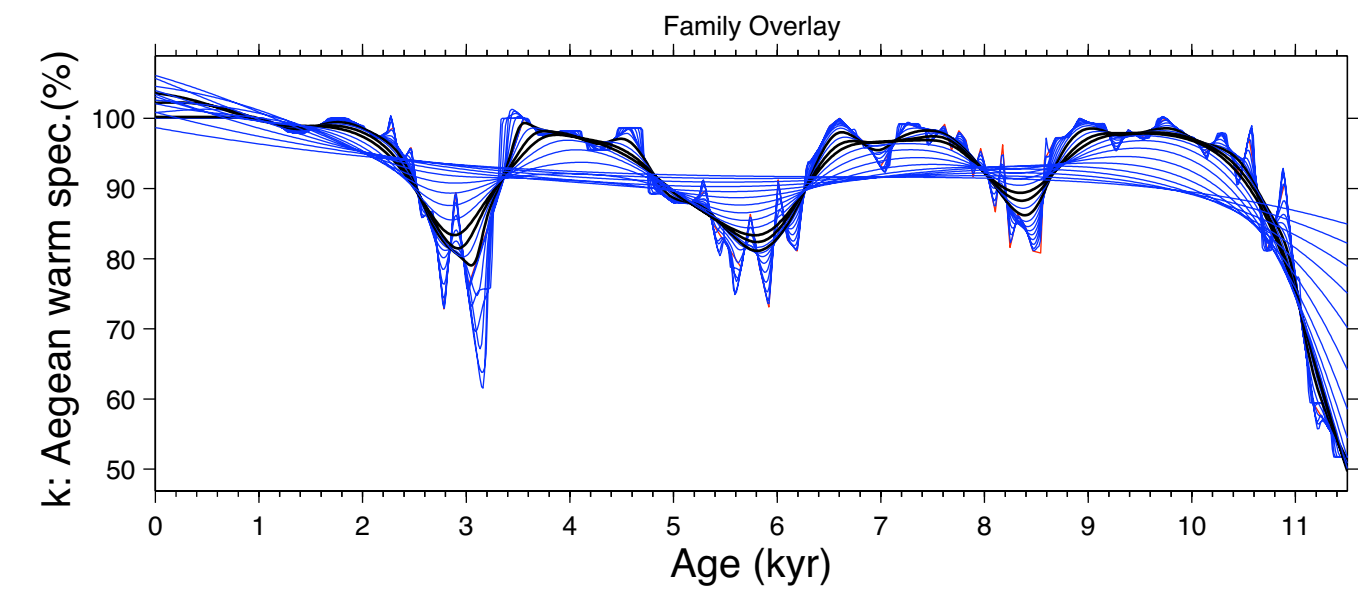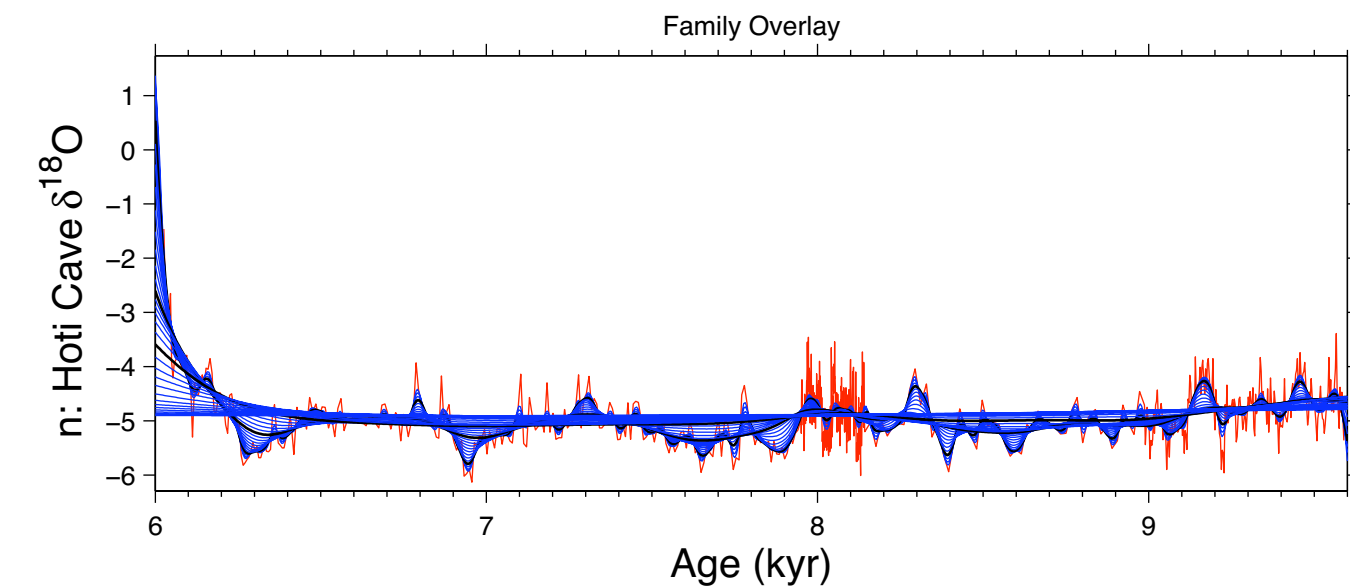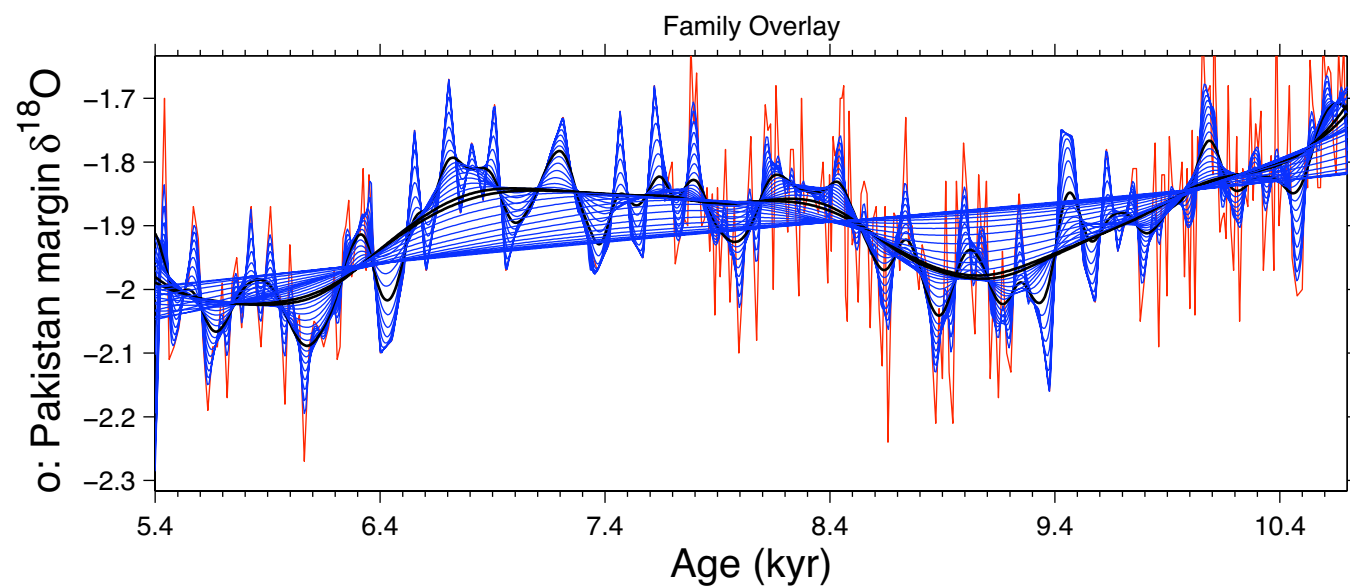
Slope SiZer Map

Curvature SiZer Map

Figure S1 continued

Family Overlay

Slope SiZer Map

Curvature SiZer Map

Figure S1 continued

Family Overlay

e: Cariaco greyscale

Slope SiZer Map

Curvature SiZer Map

Figure S1 continued

Family Overlay

Slope SiZer Map

Curvature SiZer Map

Figure S1 continued

Family Overlay

Slope SiZer Map
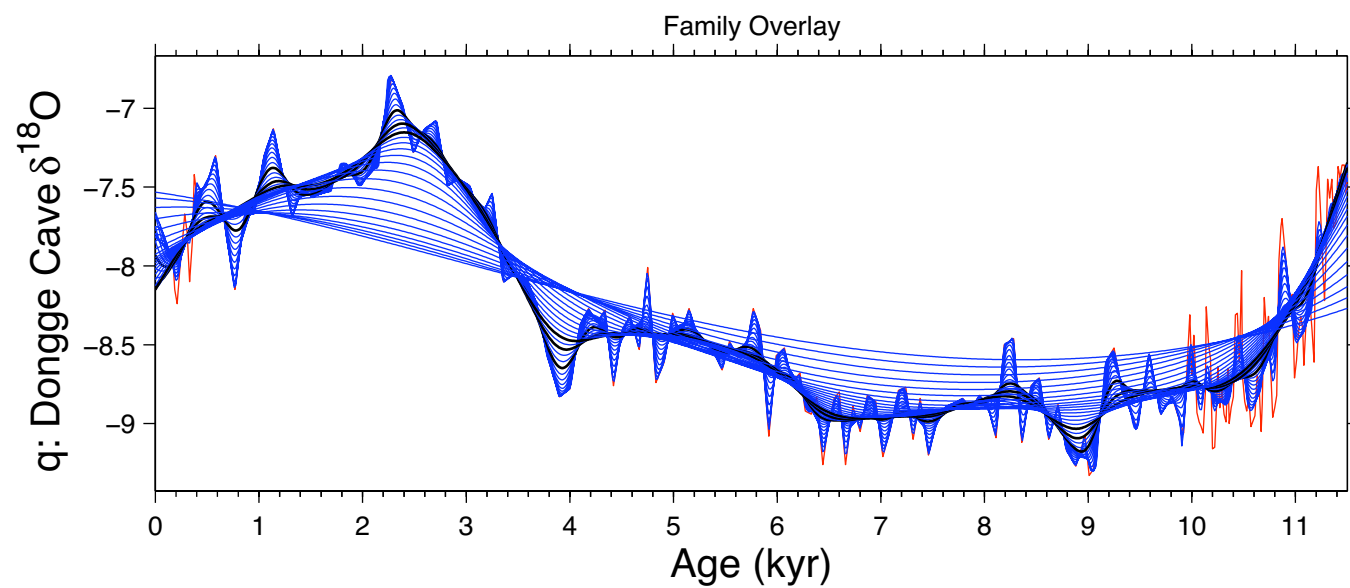
Curvature SiZer Map

Figure S1 continued

Family Overlay

Slope SiZer Map

Curvature SiZer Map

Figure S1 continued

Figure S1 continued

Family Overlay

Slope SiZer Map

Curvature SiZer Map

Figure S1 continued

Family Overlay

Slope SiZer Map

Curvature SiZer Map

Figure S1 continued

Figure S1 continued

Family Overlay

Slope SiZer Map

Curvature SiZer Map

Figure S1 continued